






RESEARCH

Open Access



Enormous headward and gully erosion in a floodplain area reclaimed for open-cast lignite mining during the July 2021 flood in the Inde River valley (Western Germany)

Johannes Keßels^{1*} , Stefanie Wolf² , Wolfgang Römer¹, Lukas Dörwald¹ , Philipp Schulte¹  and Frank Lehmkuhl¹ 

Abstract

Background The July flood 2021 at the mountain front of the Eifel-Ardenne Mountains and their foreland resulted in the flooding of the lignite mining area of Inden in Germany. The mining activities resulted in large-scale anthropogenic changes to the relief and fluvial system, leading to a landscape that is no longer adjusted to the recent process-response system. This paper concentrates on the Inde River, where lignite mining led to the relocation of a 5-km-long river section. The flood event resulted in the temporary avulsion of the Inde River into the former channel and, ultimately, in the flooding of the open-cast lignite mine Inden.

Results The flooding of the open-cast lignite mine Inden led to headwall erosion and enormous sediment mobilisation, mobilising more than half a million cubic metres of sediment within a few hours, forming a 700-m-long deeply incised channel cut. Thereby, the underlying bedrock, near-subsurface man-made structures, and former river channels influence the erosional processes to different degrees. Surface erosion is likely to be the decisive process, and subsurface erosion is likely to play a secondary role. In both cases, former channels and mill ditches were likely impacting the course of erosional processes.

Conclusions During high flood events open-cast mining sites in floodplains are endangered by enormous erosion and sediment transport within a short period of time (several hours). Understanding such complex erosion and depositional processes in open-cast mining areas could provide a blueprint for geomorphological processes and hazards in these anthropogenically shaped fluvial landscapes. Further, information on historic impact in the area is crucial to estimate potential risks.

Keywords July flood 2021, Gully erosion, Semi-circular headcuts, Fluvial geomorphology, Open-cast lignite mining

*Correspondence:

Johannes Keßels
johannes.kessels@geo.rwth-aachen.de

¹ Chair of Physical Geography and Geoecology, Department of Geography, RWTH Aachen University, Wüllnerstr. 5B, 52056 Aachen, Germany

² Institute of Hydraulic Engineering and Water Resources Management, RWTH Aachen University, Aachen, Germany

Background

Rivers are fragile ecosystems that seek a state of dynamic equilibrium between climatic conditions, morphology, geology, and their environment [1, 2]. However, worldwide, the great majority of river systems are strongly affected by human interferences and are no longer exclusively subject to natural dynamics in their hydrological behaviour [3–6]. The current landcover hardly corresponds to the natural potential vegetation [7]. In

addition, anthropogenic activities significantly alter the Earth's surface [8]. Hence, since the Palaeolithic, latest with the beginning of sedentism, humans have acted as a morphological agent [9, 10].

The influence of anthropogenic activities on the river–floodplain system as well as on the hydrological characteristics, also applies to the rivers and their catchment areas in Central Europe starting in the mid-Holocene [11]. Werther et al. [12] established the concept of the Fluvial Anthroposphere to emphasise the multi-layered interrelationship between the river–floodplain system and its importance for ecosystem services as well as for socio-cultural aspects [13]. Several studies focusing on changes of the fluvial dynamics indicate that river morphology has been affected by river straightening and channelisation, which resulted in a decoupling of floodplain and changes in flow dynamics and sediment transport [13–18]. On a catchment scale, human interferences have altered the surface and modified the hydrological cycle by deforestation, agricultural practices, increased urbanisation, and by mining and extraction activities [10, 19].

According to Chen et al. [20] open-cast mining represents one of the most significant impacts on ecological conditions [21]. In addition, open-cast mining is often associated with hydrological and morphological changes [9], with the relocation of rivers, the construction of artificial riverbeds [22] as well as with changes in relief where elevations are changed up to several tens of metres, even in the post-mining stage [23]. Additionally, open-cast mining, especially the extraction of sand and gravel, is closely linked to mining operations in riverine areas [24–27]. The landscapes affected by mining are more prone to catastrophic erosion processes [9, 28–30].

This study focuses on the Lower-Rhine Embayment (LRE) in western Germany, which has been significantly impacted by lignite (brown coal) mining and extraction of sand and gravel. The Rhenish lignite area is currently the largest lignite district in Europe, extending over an area of 2500 km² with an operating area of about 100 km², including three individual open-cast mines [23, 31]. The LRE is also the largest extraction region for sand and gravel in Germany [32]. In addition, the loess landscape of the LRE has been intensively used by agriculture for the last 7,500 years [33, 34] and is highly urbanised at the margins with one of the highest population densities in the European Union [35]. In July 2021 the southern part of the LRE was affected by the extreme flood event. This resulted in the flooding 1) of an open-cast gravel mine (Blessem) located in the nearby riverine area [36] and 2) of one of the open-cast lignite mines (Inden) where the Inde River was relocated in a 12-km-long new river channel [37]. Both of these open-cast mines have

been subject to severe erosion processes. Similar flood events are likely to occur more frequently by a persistent climate trend for this region as discussed in Tradowsky et al. [38]. This highlights the need for an understanding of the vulnerability of anthropogenic landscapes and the need to implement appropriate adaptation strategies. This paper focuses on the geomorphological processes at the Inden lignite mine, where the Inde River moved back into the old riverbed, entered the Inden mine and formed a deeply incised channel cut [39].

The deeply incised channel cut is characterised using a multidisciplinary approach that incorporates old maps, geological data sets, high-resolution digital surface models (DSMs), 3D-model visualisations calculated from it and the estimation of various erosion competencies. The objective is to identify potential morphologically relevant factors influencing fluvial erosion during extreme events.

Study area

The lignite mining area of Inden as well as the Inde River and its upper catchment extends in the south-western part of the LRE, east of the city of Aachen (Fig. 1A).

The 383 km² catchment area of the Inde River is located at the northern margin of the European low mountain ranges, the German Central Uplands [40]. This region is defined by the morphological transition between the Eifel-Ardenne-massif and the LRE. After a flow length of about 57 km, the Inde River enters the Rur River. In the lower reaches (light grey shadow in Fig. 1A), the Inde River cuts into the flat topography, which is locally affected by neotectonic faults [41] and is composed of Cenozoic fluvial and aeolian deposits [33, 42]. In particular, these are Quaternary sediments, such as fluvial gravel and sand, aeolian loess and floodplain sediments, underlain by Miocene sands with layers of lignite [31, 42].

The open-cast lignite mine Inden extends directly south of the confluence point with the Rur River (Fig. 1B). Extensive lignite mining started at the beginning of the twentieth century in the area north of Eschweiler. The Inden lignite mine began its operational phase in the 1950s and developed in an easterly direction. The lignite mining severely modified the catchment of the lower reaches. In 2005, the open-cast mine reached the original course of the Inde River. At this time, the riverbed of the New Inde River had already been established on recultivated land. The artificial river course—New Inde River—changed the river length of that original section from 5 to 12 km [43, 44].

The study area is located on the southern non-active edge of the open-cast mine and extends from the dividing point between the New Inde and the Old Inde River to the edge of the Inden mine. Figure 2 shows the situation before and after the 2021 flood. Remnants of the

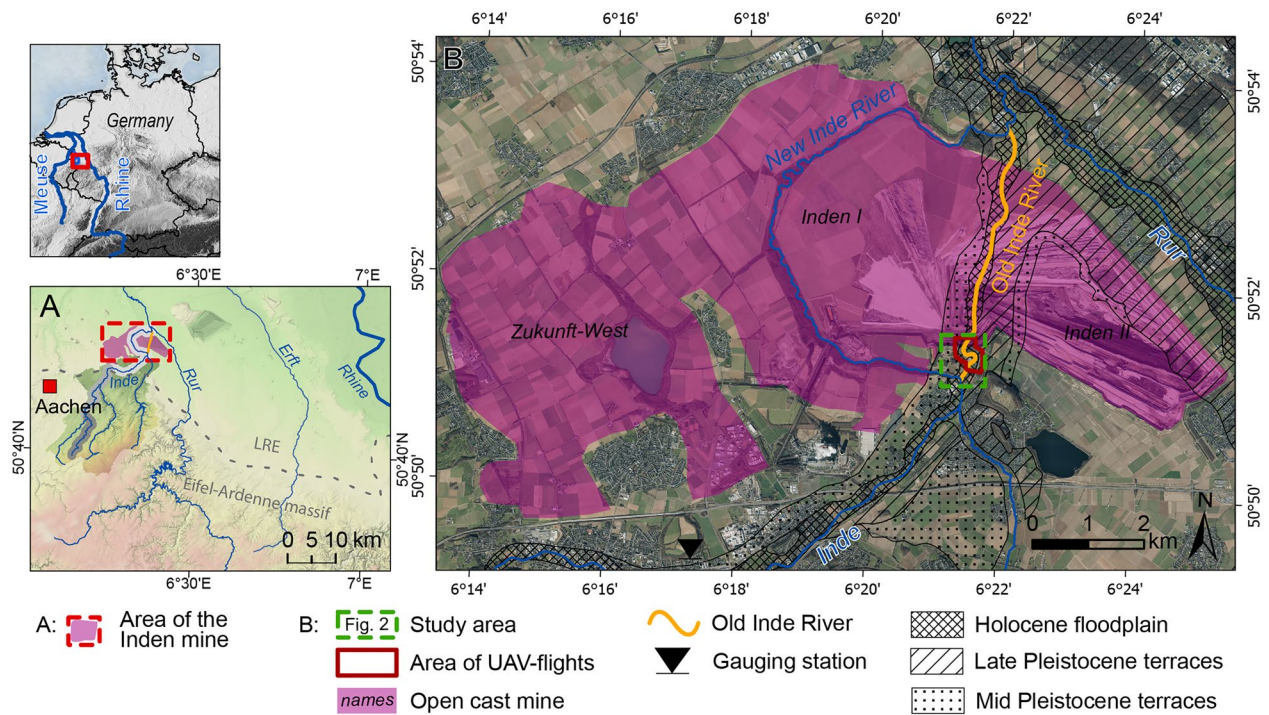


Fig. 1 **A** Location of the open-cast lignite mine Inden and highlighted by colour the upper catchment of the Inde River. **B** Aerial Image of the Inden mine and course of the relocated and former Inde River



Fig. 2 Changes in the relief of the study area before **(A)** and after **(B)** the 2021 flood event, when the Inde River had entered the open-cast mine. Symbology is adapted from Fig. 1

original river course are several ponds to retain water potentially. To the south is the relocated village of Inden-Lamersdorf with its recreational area. Along this section of the Inde River the river is kept in the riverbed by embankments designed in accordance with an HQ_{100} plus a freeboard of 2 m (Fig. 2A).

Flood event July 2021

The 2021 flood event in the Eifel Ardennes region was the result of a quasi-stationary low-pressure system passing over western Germany between the 12th and 15th of July [45]. Unusually for this region, these extremely moisture-laden air masses were pressed against the north-eastern flank of the Eifel mountains. Figure 3 shows the spatial distribution of the total precipitation and hotspots during the event. At the catchment scale, the average monthly precipitation (reference period: 1991–2020) was exceeded by a factor of 1.5 to 2 within a few hours [45]. The return period of 100 years was exceeded by far, with a possible return period of up to more than 500 years in the area of the precipitation hotspots [46].

In general, the Inde River is defined by a year-round perennial and pluvio-nival discharge regime with general high flows in winter and low flows in summer. The mean annual discharge of the Inde River is $2.60 \text{ m}^3/\text{s}$ (approximately 38 cm of water depth) at the gauging station in Eschweiler, with a mean discharge in July of around $1.4 \text{ m}^3/\text{s}$ (period: 1991–2020) [48]. After the heavy rainfall in July 2021, bankfull discharge of the Inde River resulted in the temporary avulsion of the Inde River (Fig. 4A) and activation of the former Old Inde River channel (Fig. 2B). The main paths of the water flow were across the recreational area and over the embankment at the beginning of the relocation (Fig. 4B). About 7 km upstream of the study area at the gauging station in Eschweiler, a maximum water level of 3.7 m was measured on July 15th between 6 a.m. and 7 a.m. First estimations quantify the corresponding discharge at about $270 \text{ m}^3/\text{s}$ [49]. For comparison, the highest discharge so far was $89.48 \text{ m}^3/\text{s}$ in 2007 [48].

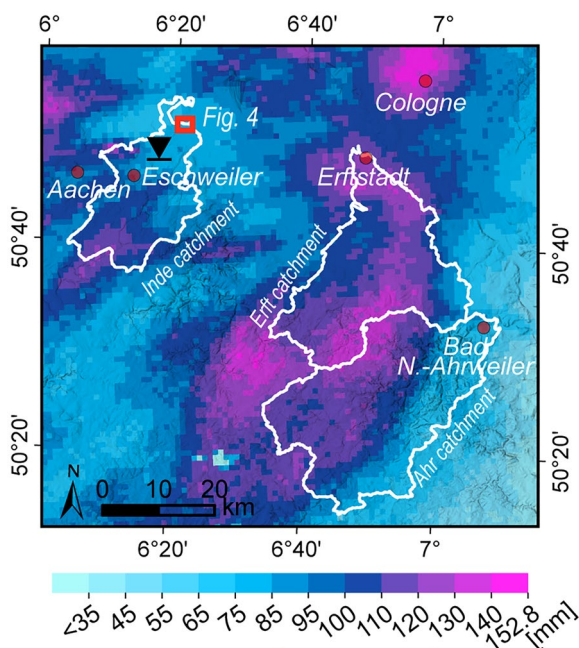


Fig. 3 Aerial total precipitation for the 13th and 14th of July 2021 (adapted after [47])

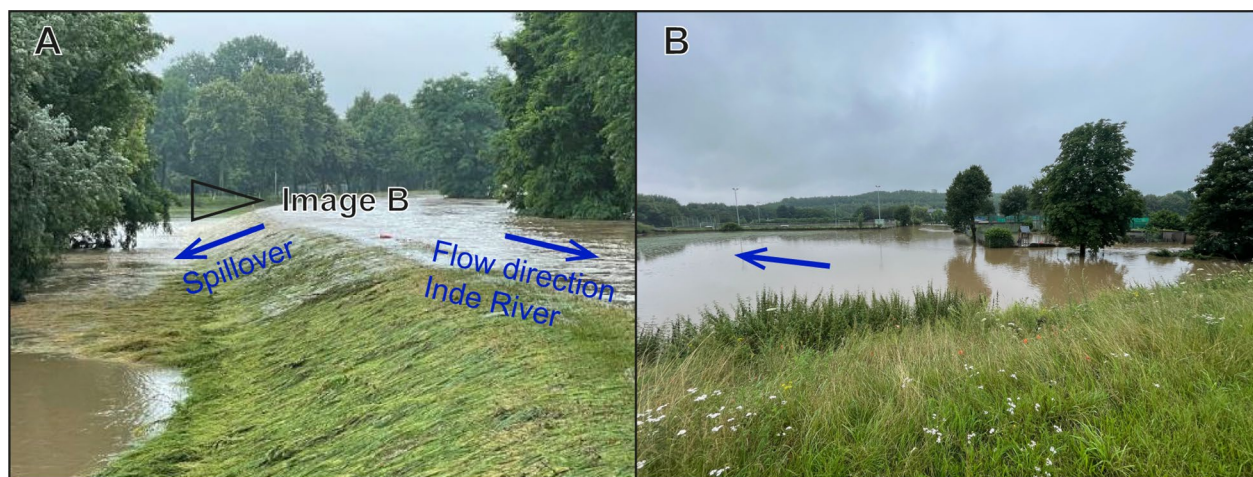


Fig. 4 Flood and remnants of the flood at the junction of the New and Old Inde River. **A** Overflow on July 15th, 2021. **B** Flooded area beyond the embankment on July 15th 2021. Locations of image **A** are shown in Fig. 2. Blue arrows indicate the overall flow direction. Photos F. Lehmkuhl

Methods

The analysis of the deeply incised channel cut is based on information from several field surveys, during which unoccupied aerial vehicle (UAV) flights were conducted. Preliminary steps prior to the morphological analysis (see subchapter III *Geomorphological processes and erosion scenarios*) are the preprocessing of the datasets from the UAV flights and the defining of the lithostratigraphic units (see subchapter I *Fieldwork/UAV flights*) and the historical assessment of old maps of this region (see subchapter II *Geological and historical data*).

Fieldwork/UAV flights

Fieldwork including UAV flights was conducted after the event on July 15th and 16th, 2021. This was followed by further field work (23.06.2021, 19.09.2021 and 16.01.2022) and mapping including second drone flights (05.06.2023) to validate and quantify the anthropogenic effort after the erosional event. This includes the documentation of different geomorphological landforms and sediment sampling. Furthermore, the timeline and action of the responsible authorities afterwards was explained to us by local guides and operators of the open-cast mine (M. Bresser, O. Day, C. Forkel, S. Witting). Surface sediment samples were collected on July 23rd, 2021, in front and after the embankment along the pathway of its overflow (Table 1). The flood mark was taken on August 4th, 2021 (Fig. S1).

For the high-resolution DSM and the orthoimages, the areas were mapped with UAV flights on the aforementioned dates. Table 2 gives an overview of the flight parameters of both field campaigns. For the UAV flights in 2021, a DJI Phantom 4 RTK was used. The UAV is equipped with a 20-megapixel digital camera, with a focal length of 8.8 mm. No ground control points (GCPs) for

georectification purposes [50] could have been taken due to time constraints and safety concerns of unstable ground after flooding-related destruction. For the 2023 flights a DJI Phantom 4 Pro V2 was used without an onboard RTK module. The camera is similar to one of the UAV models used in 2021. In order to achieve good accuracy, 7 GCPs were used. Due to the different UAV model without an onboard RTK module, used for the 2023 flights, an 80° camera angle was chosen in order to achieve a suitable perspective for a higher resolution in the post-processing [51]. The GCPs were measured with two Emlid Reach RS+dGPS devices, one set up as a base and one as a rover to collect the GCP positions. This setup reaches a mean accuracy of 1.5 mm, relative to the base. For processing Agisoft Metashape Professional 1.6.3 was used.

An additional visual comparison between the UAV-derived orthoimage and an orthoimage of the state of North Rhine Westphalia with a resolution of 1 m indicated no measurable offset between the two datasets. To achieve low distortion and no doming effect of the model, an established workflow, with iterative filtering steps of the point cloud was used, before generating the DSMs and orthoimages [52]. The resulting resolution from the orthoimages and digital surface models are listed below (Table 2).

Geological and historical data

Two datasets are combined to define lithostratigraphic units. First, various soil and geological maps are used for the near-surface layers. Second, several drill cores have been retrieved from the Geological Survey of NRW [53] for the deeper layers, which adds information, especially on the underlying Miocene rock strata. The locations of the drill cores are shown in Fig. 5. Four drill cores were of relevance for this study (see location of drill cores 1–4 in Figs. 5 and 6).

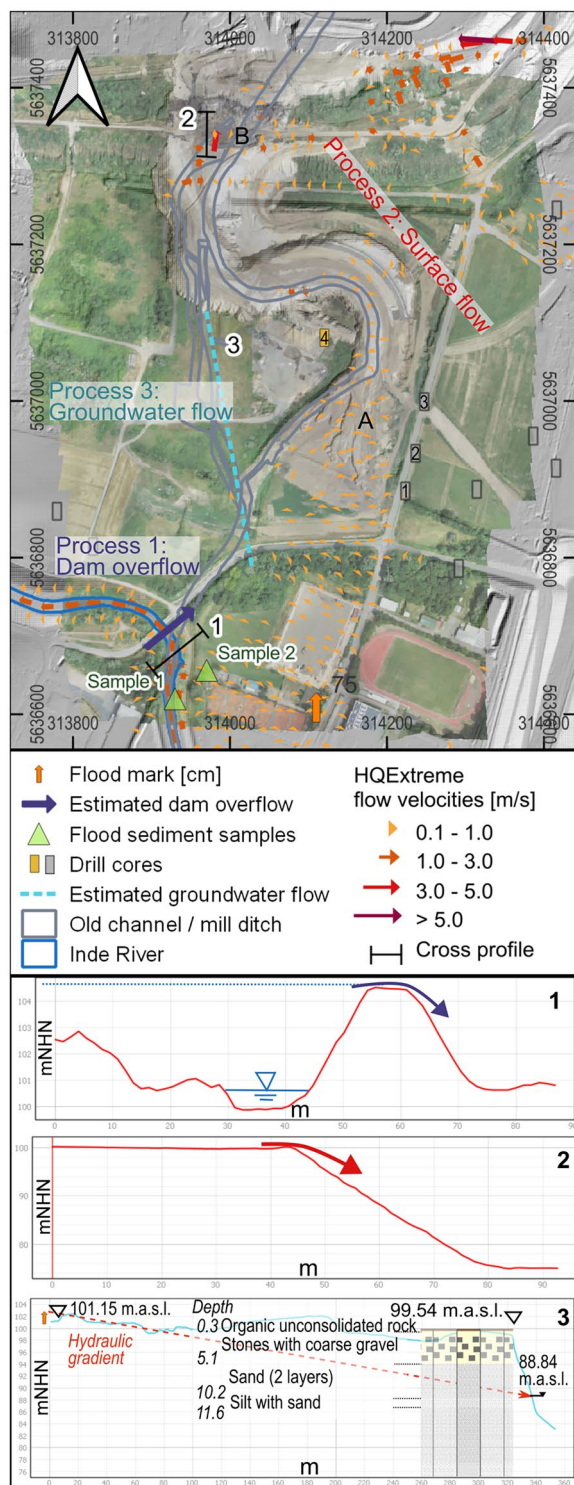
The river development in the study area and the anthropogenic influence are derived from four historical maps provided by Geobasis NRW [54]. Table 3 lists the available historical maps. The earliest map is from the Topographic Survey of the Rhineland by Tranchot from 1807/1808. The topographic map of 1998 is used for the

Table 1 Surface sediment samples

Name	Location	Mean grain size (GS)
Sample 1	See Fig. 5	181,74 µm
Sample 2	See Fig. 5	216,81 µm

Table 2 Flight parameters, dates, and resolution from the orthoimages and digital surface models and the official DEM dataset of the federal state NRW

Site	Date	Flight height [m] above ground	Image count	Camera angle [°] towards the surface	DSM resolution [cm/px]	Orthoimage resolution [cm/px]
Inde, Lamersdorf	July 16th, 2021	45	1408	90	7.68	1.92
	July 5th, 2023	80	586	80	5.72	2.86
NRW, OpenData	2018/19	DEM resolution: 1 m/px				



◀ **Fig. 5** Data basis to evaluate possible scenarios of erosion. Drill cores: GD NRW (small numbers 1–4 as in Fig. 6A), HQ_{extreme} flow velocities: LANUV NRW. Topography of the cross-profiles: pre-flood DEM. The numbers of the cross-profiles 1–3 correspond with the erosion process: (1) dam overflow at the beginning of the Inde River relocation; (2) surface erosion on the floodplain area (A) and at the brim of the open-cast mine (B); (3) worst-case scenario for subsurface flow erosion. The hydraulic gradient is estimated based on a flood mark (water level: 75cm), assuming that subsurface flow could freely leave at the brim. Silt with sand is considered to be impermeable

features, which affect the natural dynamic of the Inde River within the study area.

Geomorphological processes and erosion scenarios

For the first characterisation of the channel cut a Digital Elevation Model of Differences (DoD) is calculated based on the pre-flood DEM (Table 2) [55], representing the topography before the flood event, and the DSM from July 2021, representing the elevation directly after the flood. The DSM from July 2021 is resampled to a resolution of 1 m for comparison. Based on this DoD, referred to as DoD-flood, the volume of the eroded sediments is estimated. Further geometrical parameters for the whole channel cut as well as for different sections are determined based on 3D-models and the high-resolution orthoimages from July 2021. A second DoD has been calculated, showing the morphological and volumetric changes between the UAV-flights 2021 and 2023. All processing steps are done in ArcGISPro 3.1.1.

We distinguished the erosion event into three different processes (Table 4, Fig. 5): (1) embankment overflow: surface erosion induced directly by the overtopping of the embankment of the Inde River. Dam overflow was observed during the flood event, thus its likelihood of being one of the main processes is tested in the observed area; (2) surface flow over the flooded area is subdivided into (A) the erosional competence in the floodplain area; and (B) the erosional competence at the edge of the open-cast mine; (3) interflow in the subsurface soil resulting in internal erosion and transport (hydraulic failure such as piping, seepage and/or sapping). To evaluate the likelihood of potential subsurface soil erosion as one of the main processes, we looked at a possible worst-case scenario.

Embankment (dam) overflow (Process 1)

As the exact moment of embankment overtopping was not observed during the flood event of mid-July 2021, we assume a free overflow and an overflow depth of 10 to 20 cm as observed in the field during the event by one of the authors (Fig. 2A). The overflow velocities for a depth of 10 and 20 cm on the crest are computed

last time slice representing the situation just before the relocation of the Inde River. The historical maps provide information on the location of former river channels and historic land use. Particular focus lies on anthropogenic

after Poleni (e.g., [56]) using an overflow coefficient of 0.75. The velocity on the embankment base is computed using the Bernoulli equation. Here, we make the simplified but feasible assumption that the width of the flow stays constant, at least for the centre flow conduit, which brings the highest shear stress. Afterwards, the erosion potential is estimated using the Hjulström diagram ([57] based on [58]). It can then be compared to the present grain sizes from flood sediment samples, “Sample 1” and “Sample 2” (cf. Fig. 5).

Uncontrolled surface flow (Process 2)

During the flood of mid-July 2021, the surface flow towards the open-cast mine corresponds with the simulated flow paths of an HQ_{extreme} [59]. As flow velocities during the flood are unknown, we use the results from the simulated flow paths of an HQ_{extreme} from official flood risk maps, and estimate a mean flow velocity over the flow path. The flow path follows the old channel (Fig. 3). The erosion potential of the mean flow velocity is determined using the Hjulström diagram ([57] based on [58]). The grain sizes, which can be eroded by the mean surface flow velocity, are then compared with the grain sizes from flood sediment samples Sample 1 and Sample 2 (cf. Fig. 5). Further, water depth and flow velocity at the brim of the open-cast mine are determined from the official flood risk map to evaluate the erosion potential at the starting point of the backward erosion. To compare results obtained from the flood risk map to the assumed flow conditions during the high-energy event of mid-July 2021, water levels are compared at the location of the flood mark.

Subsurface flow erosion (Process 3)

Hydraulic failure in the soil layers is expected, when the water level within the channel drops, leading to a hydraulic gradient in the flowed through soil layer. As the geological layers are very inhomogeneous, as the drill core database of the county of NRW [53] shows, and the sampling density is insufficient to reconstruct clear layers, the possibility of subsurface flow erosion is tested on the potential worst-case scenario. Figure 5 hence shows the estimated shortest possible flow path (aquamarine line) of 315 m. The subsurface flow path starts in front of a terrain elevation due to a street. On the one hand, the estimated location of embankment overflow is nearby, on the other hand, backwater can build up in front of the terrain elevation, favouring a higher hydraulic gradient. The estimated subsurface flow path ends at the brim of the channel cut, where photos document possible piping in form of a washout fan (see Fig. 8B). The estimated subsurface flow path

starts at an elevation height of 101 m, based on the DEM1, and ends on an elevation height of 99 m a.s.l. The channel cut has an elevation height of around 88 m a.s.l.

The soil structure was taken from the drill core database of the county of NRW [53]. The drill core with the ID “DABO_198950” from 1960 [53] (cf. Fig. S2) is located nearest to the estimated subsurface flow path. Soil properties are derived from descriptions in the drill core database.

We assume the same slope in all layers towards the brim. We further assume, that the layer consisting of silt with sand acts as an aquiclude. It is also assumed, that 75 cm water accumulated on the surface in the beginning of the subsurface flow path. The value was obtained from a flood mark nearby (Fig. 5). It is assumed, that the soil saturation is at 88 m a.s.l. in the channel cut.

Using Darcy’s law (e.g., [60]), we compute the hydraulic gradient I over the corresponding length. To test the possibility of piping, I is compared to the critical hydraulic gradients $I_{crit,n}$ based on the estimated densities of the different layers, cf. Equation (2):

$$I = \frac{\Delta h}{\Delta L}. \quad (1)$$

With: Δh = difference in height of soil saturation; ΔL = estimated flow path length.

$$I_{crit,n} = \frac{\rho_{Soil}}{\rho_{water}} - 1 \quad (2)$$

With: ρ_{Soil} = density of soil layer, cf. Figure 2; ρ_{water} = density of water, 1000 kg/m.³

The average velocity v_m in the soil is computed after Darcy’s law Eq. (3):

$$v_m = k_{f,eq} \cdot I. \quad (3)$$

The equivalent k_f -value $k_{f,eq}$ over the depth profile is computed after Eq. (1) [61]:

$$k_{f,eq} = \frac{\sum_i k_{f,i} \cdot d_i}{\sum_i d_i}. \quad (4)$$

To determine if the flow velocity in the soil would be efficient to lead to particle erosion, the average velocity v_m is divided by determined porosities n after [62] (Table 5) to estimate the pore velocity $v_{p,n}$:

$$n = 0.13 + \frac{0.21}{(1000 \cdot d_m + 0.002)^{0.21}}. \quad (5)$$

As photos show signs of piping at the brim of the channel cut, $v_{p,n}$ values for the layer of organic

unconsolidated rock, the layer of stones with coarse gravel, and the layer of medium sand with fine sand is computed. Therefore, the porosity for those layers is estimated based on estimated mean grain size diameters d_m (Table 5).

Results

Geomorphological characterisation

The flooding of the Inden mine created a 700-m-long fluvial channel cut. The new base level is a lignite layer 30 m below the surface. The new fluvial landscape covers an area of approximately 65,000 m² with a maximum

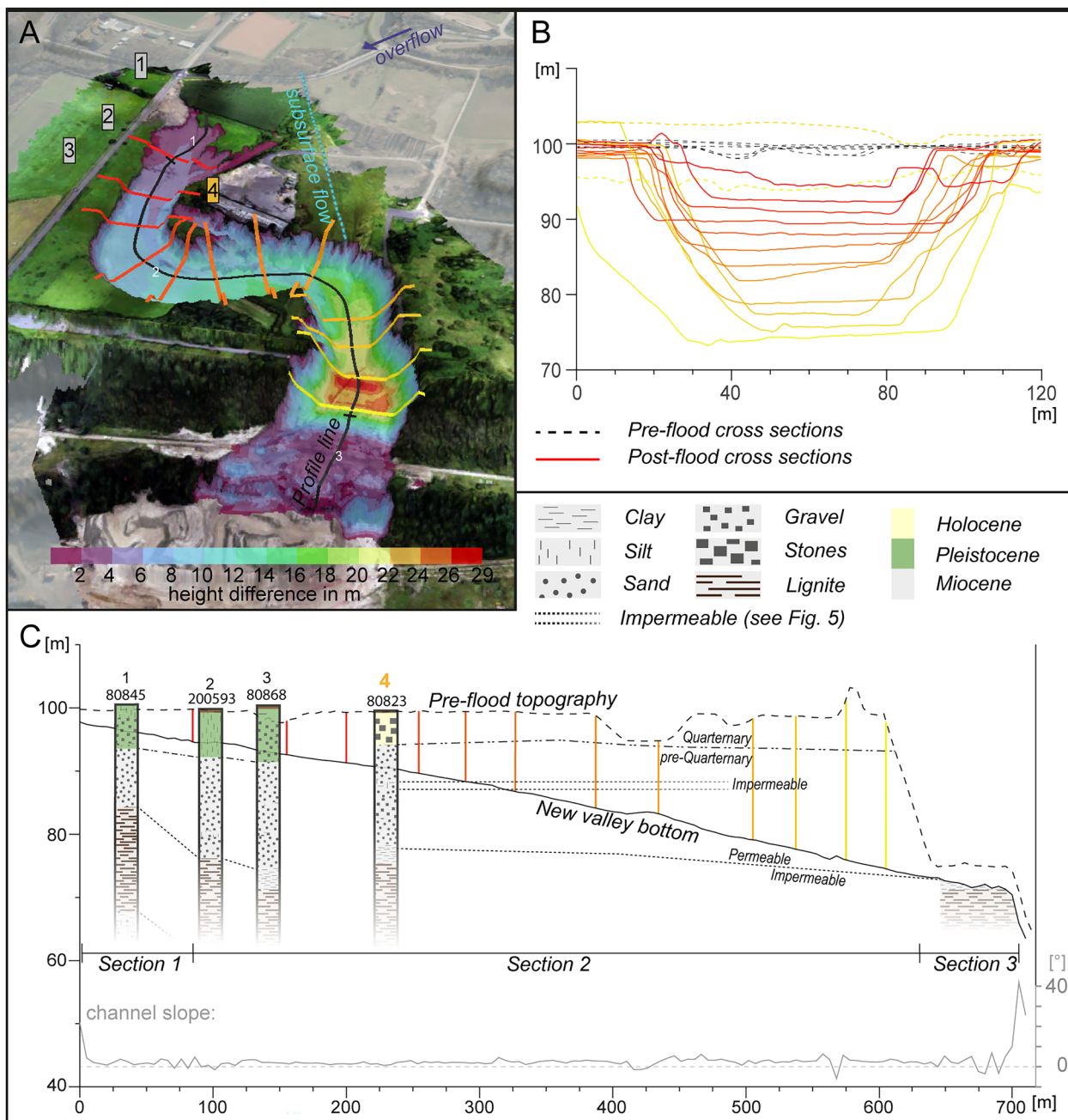


Fig. 6 **A** 3D-scene of the channel cut based on the UAV-flight images and DSM. The height differences based on the DoD-flood. The locations of the cross sections (**B**) and the profile line (**C**) are shown. The profile line in **C** shows the pre-flood topography and the new valley bottom with the corresponding slope [°]. In addition, the locations of the drill cores (1–4, symbology adapted from Fig. 5) and the cross sections along the profile are visualised. Please note that only linkages between drill cores 1–3 are possible as the layers dip to the northeast

Table 3 List of all historical maps used in this study with corresponding year and scale

Year	Name	Number	Scale
1807/1808	Topographic survey of the Rhineland by Tranchot	Nr. 78	1:25 000
1893	Prussian new survey	Nr. 5104	1:25 000
1936/45	Historical topographical map	Nr. 5104	1:25 000
1998	Topographical map	Nr. 5104	1:25 000

incision depth of 29 m at the location of the former dam crest to the Inden lignite mine. The average width of the channel cut is in the range of 60–80 m and up to about 90 m at some parts of the channel bend. Approximately 570,000 m³ of sediment has been eroded (Fig. 6).

Within the study area, the thickness and depth of the underlying sedimentary layers vary. In general, the lignite layer at the base dips to the northeast. This pattern is displayed in the drill cores in Fig. 6. In the channel cut, the top of the lignite layer occurs at an elevation of about 72 m a.s.l. around 30 m below the pre-flood topography. The alluvial deposits form the upper 1.5 m, underlain by Pleistocene gravels, while both layers have a thickness of about 6 m in the southeastern part, the thickness decreases to the northwest. Between the lignite layer and the Pleistocene gravels, Miocene sand is interbedded, which mainly consists of medium sand with further proportions of fine and coarse sand to fine gravel.

Three sections are distinguished along the profile (Fig. 6C). (1) The area of the first 80 m with a total incision of less than 4 m. This section is characterised by semi-circular headcuts of about 8 to 15 m width, indicating the zone of active headward retreat. These headcuts form several upstream expanding fingers, with width-to-length ratios varying from 1:1 to 1:4. The profile form of the headcuts displays a vertical scarp with some overhanging material, which is still stabilised by the vegetation cover. The different shaped and sized headcuts are formed in the top cohesive floodplain deposits above the Pleistocene gravel layer, which still partly covers the underlying sandy deposits (Fig. 7). Dissection by the flood water resulted in the undercutting of the soft material of the alluvial deposits but was retarded at the 4- to 5-m-thick Pleistocene gravel. The transported gravel has a mean clast size of 3 to 4 cm, though few clasts may have a maximum length of 12 cm with short intermediate axes of 3 to 4 cm (Fig. 7D).

(2) Further downstream, the different fingers in section 1 of the channel cut converged into a box-shaped, deeply incised channel about 550 m long. The gradient of the channel decreases to an average of 2.2°. In this section, the channel cuts into the Miocene sands up to the depth of the lignite layer (Fig. 6C), resulting in height

differences of more than 8 m (Fig. 6A). Figure 6B shows the corresponding cross sections, which indicate the predominant box-shaped channel form. The sidewalls are almost vertical in the upper part, composed of alluvial deposits, and have still steep angles of more than 50° within the Pleistocene gravel layer. The lower sidewalls are characterised by angles between 30° and 50° and consist of material slumped from the upper sidewalls (Fig. 6A). In addition, between cross sections 7 and 9, material from debris flows were deposited in small alluvial fans on the valley floor. The debris flows originated in the western sidewall, resulting in various-sized V-shaped scars in the upper sidewalls (Fig. 8A, B). At two locations in section 2, there are further semi-circular headcuts in the upper 2–3 m of the sidewalls. One is just north of the former paper factory, and the other is on the left sidewall at the end of section 2. Both are remnants of an early stage of the channel cut development before the increased incision into the Miocene sand began.

(3) The third section starts with the outflow into the open-cast mine. The cross sections widened, and sandy deposits of 3 to 5 m thickness, which overlay the lignite layer, were eroded (Fig. 8C, D). It has been estimated that inflow into the open-cast mine produced a lake with 1.5 million m³ of water (C. Forkel, oral communication).

The flood event resulted in enormous damage to the open-cast mine Inden during the flooding and was accompanied by significant challenges in the post-flood recovery process. Figure 9 shows the situation in July 2023. Considerable effort was made to stabilise the newly eroded channel to prevent further erosion. This includes sheet pile walls, more than 1400 concrete lego bricks, and channel modifications (Fig. 9B). Over the two years, approximately 290,000 m³ of material were moved within the study area.

Historical river courses and land-use

The analysis of the historical maps reveals the land use and the stream development from the nineteenth century onwards. Already 200 years ago, a paper mill and an associated mill ditch, which cuts off the meander bend, were mapped at the inner part of the channel bend, indicating the early influence on the fluvial dynamic in this area. Further time slices (1893–1998) document the additional construction and the abandonment of various hydraulic engineering structures stabilising the riverbank and the riverbed. The topographical map of 1936/1945 shows a railway line to the factory site including a bridge over the Old Inde River. This construction had already been removed by 1998 (Fig. 10). Different parts of this river section were straightened and modified to varying degrees at different times. Latest since 1893, a weir

Table 4 Overview of possible erosion scenarios leading to observed gully formation, which have been tested on their likelihood to be the main driver

Process	Reference to figures	Location	Decisive or worst-case scenario	Data basis	Inaccuracies
Embankment (dam) overflow	Figure 5, Process 1, Fig. 4 A	Beginning of the Inde River relocation	Dam overflow of 20 cm	Observations, geometry based on DEM 1, surface soil samples collected after the flood	Only rough observations, time of observation in relation to peak discharge is not clear
Uncontrolled surface flow	Figure 5, Process 2 A	Overland flow path determined by the flood risk map related to an HQ _{Extreme}	HQ _{Extreme} based on flood risk maps	HQ _{Extreme} based on flood risk maps, surface soil samples collected after the flood	HQ _{Extreme} based on flood risk maps is below flood event of mid-July 2021 and incorporates unknown model inaccuracies
Subsurface flow erosion	Figure 5, Process 2 B Figure 5, Process 3, Figure 8 B	At the brim of the open pit mine Shortest flow path from area of measured flood mark to observed washout fan in gully erosion	HQ _{Extreme} based on flood risk maps Shortest flow path along former channels, drill core (4) representing possible channel sediments, nearest flood mark Hydraulic gradient from possible max. (according to flood mark) to washout fan. The hydraulic gradient is estimated based on a flood mark, and assuming, that subsurface flow could freely leave at the brim. The fourth layer, silt with sand is assumed to be impermeable	HQ _{Extreme} based on flood risk maps, soil samples Flood mark, drill core (4)	HQ _{Extreme} based on flood risk maps Only one available flood mark and drill core, thus information on permeable and impermeable layers, and hydraulic gradient are sparse

Table 5 Estimation of porosity in layers of potential erosion due to subsurface flow. Layers are shown in Fig. 5. Properties are derived after [63] and [64] based on descriptions in the drill core database (see also Fig. S2)

Layer	Function	Estimated k_f [m/s]	Estimated ρ [t/m ³]	Estimated d_m [m]	Estimated n [-]
Organic unconsolidated rock	Top layer	5×10^{-7}	1.52	0.05×10^{-3}	0.5
Layer of stones with coarse gravel	Permeable	1×10^{-1}	1.68	10×10^{-3}	0.3
Medium sand with fine sand	Permeable	2×10^{-4}	1.56	0.2×10^{-3}	0.4
Coarse sand with medium sand	Permeable	2×10^{-3}	1.60	0.2×10^{-3}	0.4
Silt with sand	Impermeable	1×10^{-6}	1.60		

highly controlled the discharge regime within the meander bend. However, over the last 200 years, this meander bend of the Inde River has shown a downstream translation of more than 50 m (Fig. 10). The modern paper factory was built on the coarse point bar made of gravel, which was active at the beginning of the nineteenth century.

Erosion scenarios

Process 1 tests the erosion capacity directly at the beginning of the water inflow into the floodplain area (Fig. 4 A). The embankment overflow leads to flow velocities at the base ranging between 8.5 m/s to 9 m/s for water

levels of 0.1 m to 0.2 m at the embankment crest. According to Hjulström diagram ([57] based on [58]) grain sizes up to cobbles and boulders can be entrained by this flow as suspended load. Hence, surface erosion is highly likely already during this process.

At the edge of the open-cast mine, water levels are around 0.7 m for an HQ_{extreme} . Corresponding flow velocities are about 1.8 m/s at the top and up to 3.9 m/s at the lower end of the slope [59]. At flow velocities of 1.8 m/s, particles between 3 μm and 22 mm can be eroded. At 3.9 m/s, all particles up to around 130 mm can be eroded. During the initial stage of headward erosion, this condition is sufficient to erode the top cohesive

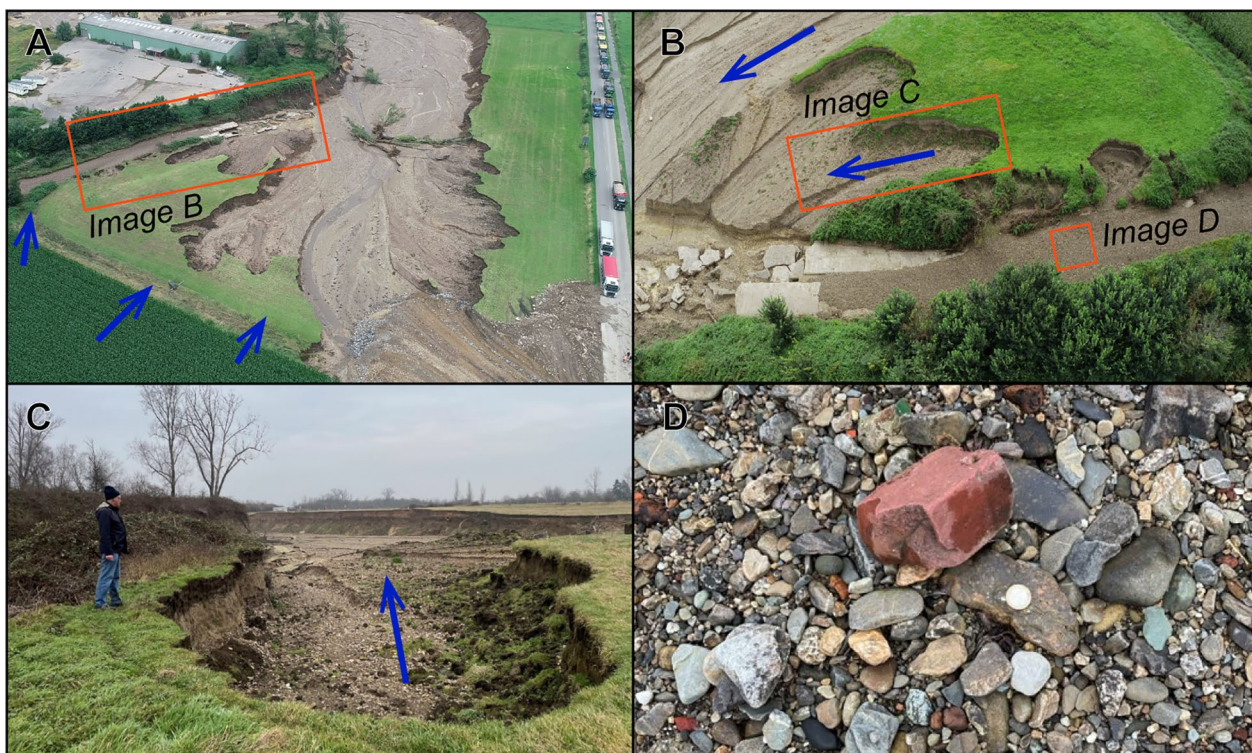


Fig. 7 **A** Aerial Image of the headcuts (section 1). **B** Semi-circular headcuts of various shapes. **C** Headcut in the upper alluvial deposits and Pleistocene gravel with vertical to vegetated sidewalls. **D** Sedimentation of gravel. The one-euro coin indicates the size. Blue arrows indicate the overall flow direction. **A, B:** IWW; **C, D:** F. Lehmkuhl

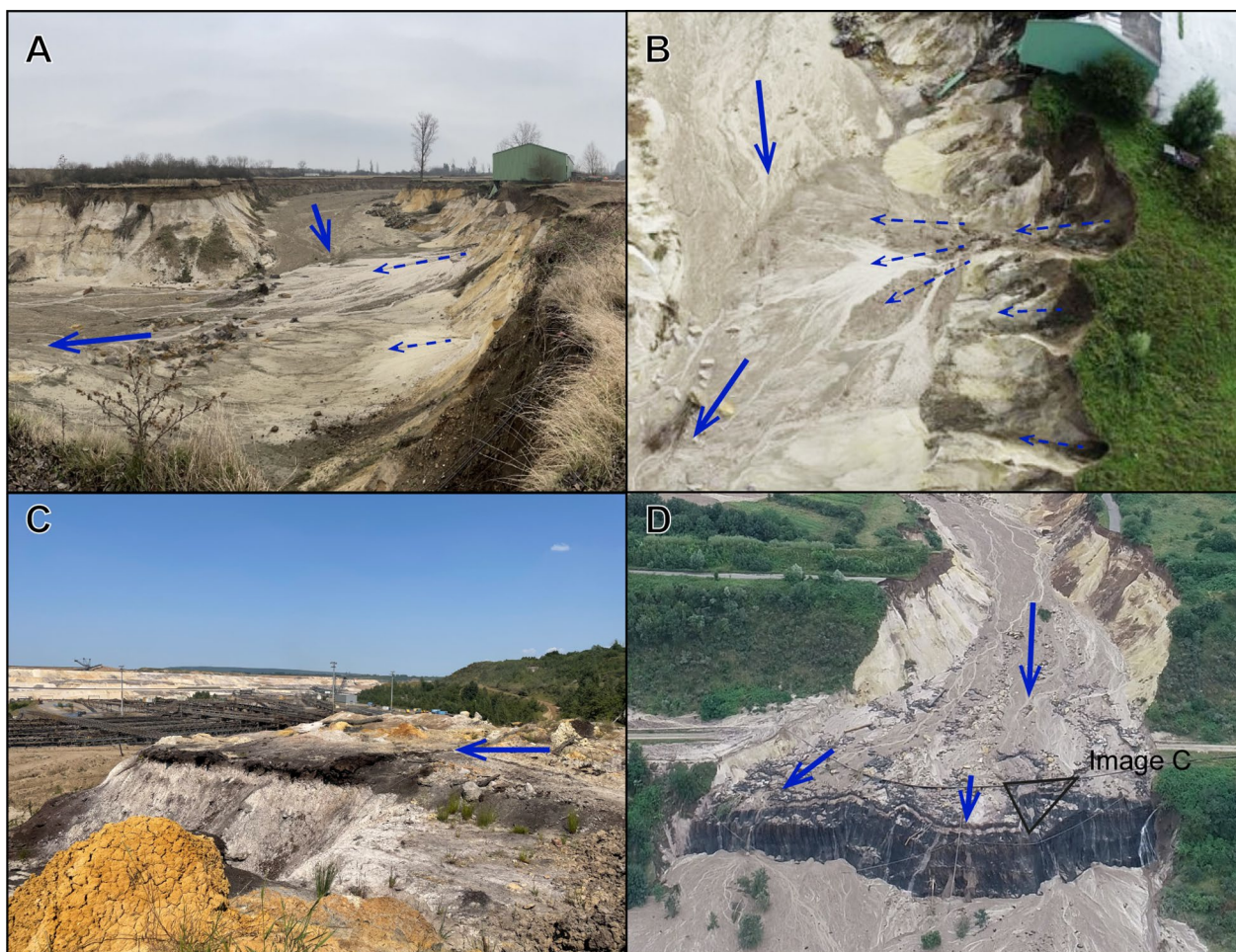


Fig. 8 **A** View into the channel cut looking upwards (section 2). **B** Aerial image of the left sidewall of section 2 showing the accumulated fans and semi-circular cuts. **C** Surface of the lignite layer and height of the new base level. **D** Aerial image of section 3. Blue arrows indicate the overall flow direction, and blue dashed arrows indicate the fans accumulated on the new valley floor and scars in the upper sidewalls. **A, C:** F. Lehmkühl; **B, D:** IWW

floodplain deposits, which consist of sediments with grain sizes of silt and fine sand and the Pleistocene terrace material of coarse gravel. The same is true for the whole study area, where the mean velocity of the surface flow is 0.4 m/s, referring to the simulated flow paths of an HQ_{extreme} [59]. Based on the Hjulström diagram, particles from 20 μm up to 1 mm can be eroded ([57] based on [58]). Therefore, the surface flow is sufficient to erode the material collected in Sample 1 and Sample 2, which have a mean grain size diameter of 216.8 μm (0.22 mm) and of 181.7 μm (0.18 mm), respectively, which equals the grain size of fine sand to medium sand. However, the flood mark taken at a fence at the recreational area (Fig. 5) indicates higher water levels than assumed in the official HQ_{extreme} scenario (measured: 75 cm, assumed: 57 cm). For this reason, velocities and erosion capacities are expected to exceed the HQ_{extreme} .

Small alluvial fans cover the bottom of the channel at its southern rim, indicating later gully erosion and accumulation in the channel from the steep bank. We assume that this later process was induced by subsurface flow including piping in the gravel layer. In order to test whether piping may be a reasonable process subsurface flow has been calculated from an area of the backwater to the channel (Fig. 5, Process 3). The hydraulic gradient has been determined from Eq. 1:

$$I = \frac{\Delta h}{\Delta L} = \frac{101.15\text{m} + 0.75\text{m} - 88.84\text{m}}{315\text{m}} = 0.041.$$

As Table 6 shows, the hydraulic gradient based on the drill core is smaller than the critical hydraulic gradients of the layers. Therefore, hydraulic failure or piping is seen as unlikely.

To determine the pore velocity, the equivalent k_f -value of the drill core is computed according to Eq. 3:

$$k_{f,eq,DC} = \frac{0.3m \cdot 5 \cdot \frac{10^{-7}m}{s} + 4.8m \cdot 1 \cdot \frac{10^{-1}m}{s} + 4.3m \cdot 2 \cdot \frac{10^{-4}m}{s} + 0.8m \cdot 2 \cdot \frac{10^{-3}m}{s} + 1.4m \cdot 1 \cdot \frac{10^{-6}m}{s}}{11.6m} = 4.16 \cdot \frac{10^{-2}m}{s}$$

The mean value therefore is:

$$v_m = k_{f,eq} \cdot I = 4.16 \cdot \frac{10^{-2}m}{s} \cdot 0.041 = 1.72 \cdot 10^{-3}m/s$$

Pore values are listed in Table 6. According to Hjulström [58] at those velocities, transport of silt and erosion of unconsolidated mud is possible.

Discussion

The case study shows the formation and migration of head-cuts and, simultaneously, the development of a knickpoint in an extremely anthropogenically shaped environment. The long-term human impact on the study area is observable in the old maps and the present-day landscape. The analysis of the historical maps illustrates, for the last 200 years, both the natural meander dynamics and the early anthropogenic impact on the riverine area at our study site. In particular, during the transition from the 19th to the twentieth century, the Inde River was massively stabilised and canalised. It should be noted that anthropogenic structures, especially the mill ditches or the railway tracks, have reshaped parts of the topography several times over the last 200 years and severely disturbed the near-surface subsoil. The results are consistent with other studies in the same catchment area and region [65, 66]. However, these structures are not directly visible on the modern surface or existing soil and geological records. In modern times, the progress of the Inden open-cast lignite mine is significantly altering the hydrological network by relocating the former 5-km-long section of the Inde River around the mining pit. This relocation aligns with the criteria of the European Water Framework Directive and aims to fulfil the pre-industrial characteristics of the Inde River. This near-natural state has been confirmed in various studies [43, 44]. This targeted characteristic is in line with Flatley et al.'s [22, 29, 67] criteria for making relocated river segments as resilient to flood events as possible to minimise the risk of embankment failures, damage to nearby infrastructure, and flooding of open-cast mines. However, the 2021 flood event reveals the hydraulic limitation of the New Inde River for an HQ_{100} event, as a higher discharge tends to divert the water to flow several metres further upstream into the old riverbed, despite the additional freeboard at the exact junction between the Old and New Inde River. The 2021 flood event shows that the vulnerability to extreme events depends on the lowest safety measures in the broader area.

At the 2021 flood event, shortly after the embankment overflow, the inflow into the open-cast mine

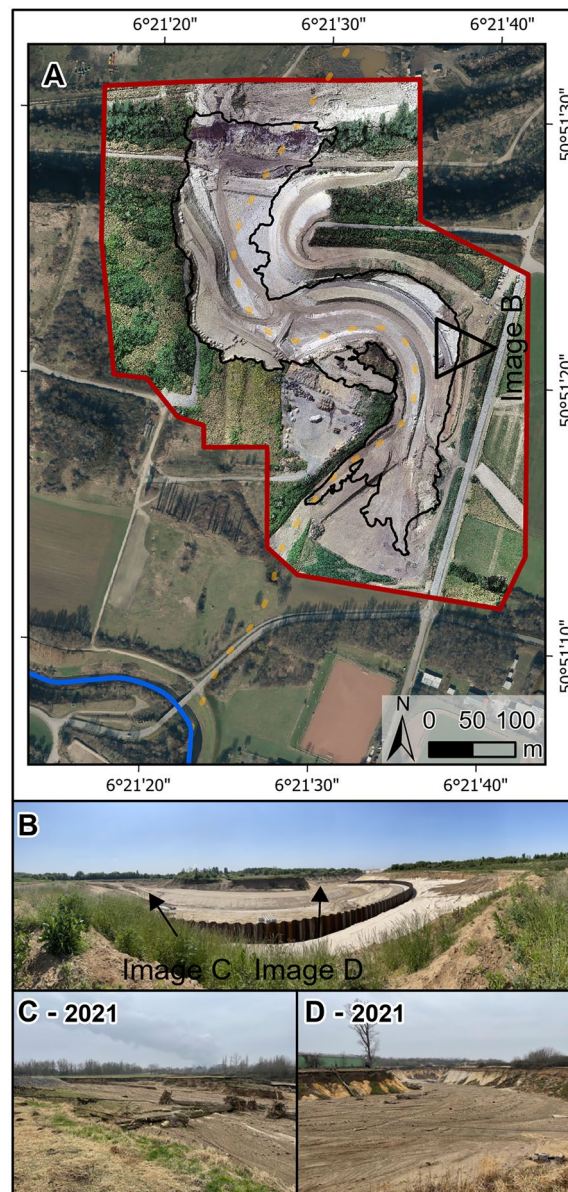


Fig. 9 Map of the study area for 2023 (A). The visualisation is based on the orthoimages and hillshades calculated from the DSMs from the second drone flight listed in Table 1. Symbology is adapted from Fig. 1. The black line marks the extent of the channel cut, as in Fig. 2B. The images below contrast the study area in July 2021 (C and D) and July 2023 with flood protection measures under construction (B). Photos: F. Lehmkuhl

started at two points, as marked on the flood risk map of NRW. Both flow paths occurred at breakthroughs for roads through the dam to the open-cast mine Inden (Fig. 5). In the final stage, the runoff into the open-cast mine was concentrated in one drainage path, from which the observed gully erosion started as the process of the knickpoint development. Further incision followed the meandering pattern of the Old Inde River and the historical river courses rather than the shortest flow path. Previous flow trajectories are reflected by the pronounced headcuts in sector 2 but are decoupled from the main channel cut by further incision as headward migration continues. The incision rate decreases within the gravel-rich layer, protecting the sandy sublayer. This is reflected by the higher length-to-width ratios of the individual headcuts due to prolonged inflow and is a typical feature of the headcut retreat [68]. The erosion of approximately 570,000 m³ of sediments represents a unique event without precedent in the entire region so far. The renewed aerial survey of the gully in 2023 (Fig. 9) indicates that huge amounts of sediments have been relocated in the

aftermath, changing the channel’s morphology, in addition to several protection measures.

The morphological characterisation of the deeply incised channel cut is susceptible to various potential inaccuracies. Common errors from SfM-UAV Photogrammetry products are doming error and vertical and horizontal offsets. To minimise these, we followed an established and well-proven processing workflow [51] with the use of an RTK UAV in 2021 and GCPs in 2023 (cf. 1 Fieldwork/UAV-flights). These inaccuracies are lower than the spatial resolution values (Table 2) and are, therefore, negligible, as the DSMs were down-sampled to a matching resolution of 1 m.

The assessment of the erosion potential of the flood is based on the processes of the embankment overflow (Process 1, Fig. 4A), the uncontrolled surface flow in the entire study area (Process 2) and the subsurface flow (Process 3). Estimating the effectivity of the erosion processes involves several assumptions, which are explained in detail in the methods part. As the flood of mid-July 2021 was an unexpected extreme event, data

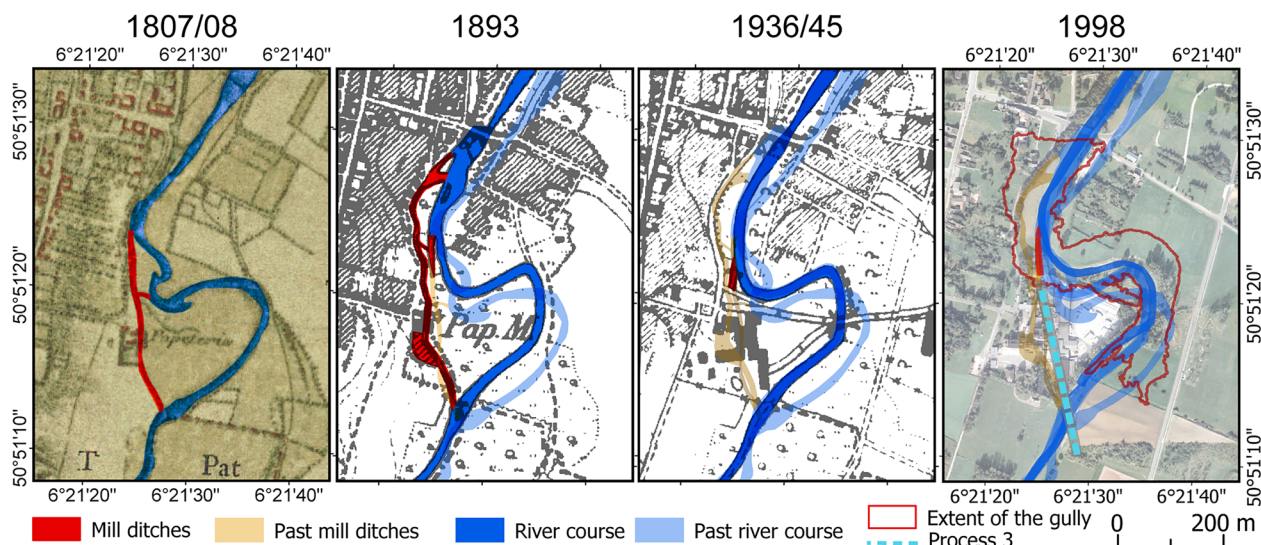


Fig. 10 Historical maps of the study area for the last 200 years showing the development of the early paper mill to the modern factory and the different artificial and natural river courses of the former Inde River

Table 6 Results of testing the possibility of subsurface erosion by the hydraulic gradient and the pore velocity

Possibility of piping/erosion tested by...	Hydraulic gradient I		Pore velocity v _p	
	I _{crit}	Result	v _p [m/s]	result
Organic unconsolidated rock	0.52	Low possibility of piping, I < I _{crit}	3.45 × 10 ⁻³	Transport of silt and erosion of unconsolidated mud
Stones with coarse gravel	0.68		5.75 × 10 ⁻³	
Medium sand with fine sand	0.555		4.31 × 10 ⁻³	
Coarse sand with medium sand	0.6			
Silt with sand	0.6			

collection was ad hoc and restricted by safety concerns. As data were perishable, missing values, or comparative data could not be collected during this study. Thus, observations during the flood event, as well as available perishable data, such as the flood mark and the sediment samples, are of high value but come with limitations in comparison to data from regular fieldwork. The accuracy of the flood mark is expected to be in the magnitude of decimetres, and the sediment samples are point values as well. Also, the spacing between existing drill cores is insufficient to reconstruct exact layers for assessing the subsurface flow. Additionally, the properties of single layers are unknown and have been estimated based on literature (cf. Table 5). Further, peak discharge and flow velocities are unknown, and the single flood mark cannot be extended to a larger area due to possible damming. Thus, we use the flood risk map and the values for an HQ_{extreme} to assess erosion processes. Nevertheless, the data basis is sufficient to estimate the likeliness of possible erosion processes. For Process 2, results indicate surface erosion is likely due to embankment overflow and uncontrolled surface flow. If surface erosion is likely based on values for an HQ_{extreme} event, it is very likely for the flood event of mid-July 2021, as values exceeded an HQ_{extreme} event [49, 69]. Further, the subsurface flow is unlikely to be the main driver in the assumed worst-case scenario, thus we assume, that results are on the safe site. However, the by far highest erosion potential occurred at the edge of the open-cast mine, where the headward erosion started. Due to the high precipitation amounts and the measured water level at the gauging station in Eschweiler, as well as due to the information from the flood mark, which exceeds the conditions of an HQ_{extreme} event, we define both erosion scenarios as the baseline for the erosional competence during the flood event.

The formation and migration of the headcuts (Fig. 7) as part of the gully erosion are generally associated with overland flow, subsurface flow, and mass movement [70]. However, many theoretical studies about headcut formation and migration have focused mainly on the erosional competence by overland flow and plunge pool erosion [71, 72]. In contrast, Wilson [73] points out that subsurface flow can be the dominant process for gully erosion. This is in agreement with the observations by Nichols et al. [74], who also points out that the shape analogy between soil erosion by subsurface flow and plunge pool erosion due to possible subsequent slumping and bank failure complicates the identification of the erosional processes after an event. During the same flood event, similar semi-circular headcuts were formed in an adjacent catchment area at the gravel pit Blessem and are already discussed in terms of the dominant morphological process (e.g., [36]). At Blessem, the primary contribution of

subsurface flow erosion as a morphological agent forming the semi-circular headcuts is initially stated by Mohren et al. [75] and Clostermann & Lisiecki [76]. Blessem and Inden are comparable in terms of the morphological forms created during the event, the magnitude of soil loss and almost in the duration of the erosion event. Even though the case study of Blessem is one of the few comparable study sites, as many other studies concentrate on the long-term analysis of gullies with considerably reduced process rates [74] in both active open-cast mines [77, 78] or post-mining landscapes [79–81], the erosion events at Inden and Blessem differ in their morphological characteristics concerning the process extent, direction, and depth of erosion, as well as their geological setting. While the geology at Blessem is characterised by thick Pleistocene gravel layers covered by alluvial sediments up to about 3 m, at Inden, the Pleistocene gravel layers are less thick and underlain by more erodible Miocene sandy sediments.

At our study site, Inden, there is no comparable evidence to that of Blessem, which shows that processes of subsurface erosion predominantly contributed to the development of the deeply incised channel cut. However, alluvial fans and V-shaped scars occur especially within section 2, all of which emerge from or are located at the right flank of the valley (Fig. 8A, B). This corresponds with the areas where the former mill ditches were located and flowed back into the main channel of the former Inde River (Fig. 10). Localised zones with high pore-water pressures may initiate material removal by seepage, landsliding, or gully erosion and act as zones for convergence of subsurface flow. In addition, the decay of roots and burrows of animals may contribute to localised zones of high interflow, which, in association with steep sidewalls and headcuts, may result in localised erosion by piping. These secondary forms indicate that the historical anthropogenic features are, subordinately, controlling modern erosional processes.

Conclusion

The study area of Inden provides an example of enormous gully erosion during a single extreme flood event in an environment that has been utilised and shaped by humans for at least 200 years, intensified by today's lignite mining. It can be conceptualised as a blueprint for the rapid development of a gully and its headcuts during a single extreme flood event, as a consequence of open-cast mining activities in the floodplain area.

The flood resulted in the temporary avulsion of the Inde River and led to the activation of the former river channel prior to the relocation. The flooding of the mining site produced a large base-level change over a short distance, resulting in a steep local gradient. This,

in turn, favoured increased stream power that forces intense and rapid headwall and gully erosion, removing huge amounts of Quaternary and Miocene sediments for several hundred metres within a short time period (several hours).

The boundary conditions enabling rapid erosion are, first and foremost:

- The relief (base-level change),
- The lithostratigraphy (composition and thickness of sediments: flood loam, gravel and sand) and
- The location of past river channels, which appear to influence the dominant direction of the gully erosion.

In addition, (subsequent) erosion was favoured along buried structures such as past mill ditches, railroads and industrial remains.

This study emphasises the need to understand the current landscape as the result of complex interplay between historical and modern human activities as well as morphological and geological structures in the subsurface. The extreme gully erosion development occurred in an anthropogenically highly modified landscape, where both past and recent, natural as well as anthropogenic processes interact.

Abbreviations

m a.s.l. Metres above sea level
LRE Lower Rhine Embayment

Supplementary Information

The online version contains supplementary material available at <https://doi.org/10.1186/s12302-024-00997-4>.

Additional file 1.

Acknowledgements

We thank V. Esser for her help during the sediment sampling and E. Vonden and J. Dressen for obtaining the flood marks. M. Formen and H. Schulten helped improve the figures. Furthermore, several local experts (M. Bresser, O. Day, C. Forkel, S. Witting) provided valuable information on the two sites at the Inde and Erft Rivers. We highly appreciate Bernhard Becker's valuable input and help with estimating the subsurface flow. We further thank the two anonymous reviewers.

Author contributions

Conceptualisation: JK, FL; methodology: JK, FL, SW, LD, WR; data analysis: JK, SW; writing—original draft preparation: JK, FL, SW, LD; writing—review and editing: FL, WR, PS, AW, JK; visualisation: JK, SW; supervision: FL, WR, PS. All authors read and approved the final manuscript.

Funding

Open Access funding enabled and organized by Projekt DEAL. Not applicable.

Availability of data and materials

The datasets used and analysed during the current study are available from the corresponding author upon reasonable request.

Declarations

Ethics approval and consent to participate

Not applicable.

Consent for publication

Not applicable.

Competing interests

The authors declare no competing interests.

Received: 29 May 2024 Accepted: 22 September 2024

Published online: 14 October 2024

References

- Allen MR, Ingram WJ (2002) Constraints on future changes in climate and the hydrologic cycle. *Nature* 419:224–232. <https://doi.org/10.1038/nature01092>
- Hack JT (1960) Interpretation of erosional topography in humid temperate regions. *Am J Sci* 258:80–97
- Nilsson C, Reidy CA, Dynesius M et al (2005) Fragmentation and flow regulation of the world's large river systems. *Science* 308:405–408. <https://doi.org/10.1126/science.1107887>
- Grill G, Lehner B, Thieme M et al (2019) Mapping the world's free-flowing rivers. *Nature* 569:215–221. <https://doi.org/10.1038/s41586-019-1111-9>
- Best J (2019) Anthropogenic stresses on the world's big rivers. *Nat Geosci* 12:7–21. <https://doi.org/10.1038/s41561-018-0262-x>
- Macklin MG, Lewin J (2019) River stresses in anthropogenic times: large-scale global patterns and extended environmental timelines. *Prog Phys Geogr Earth Environ* 43:3–23. <https://doi.org/10.1177/0309133318803013>
- Kaplan JO, Krumhardt KM, Zimmermann N (2009) The prehistoric and preindustrial deforestation of Europe. *Quatern Sci Rev* 28:3016–3034. <https://doi.org/10.1016/j.quascirev.2009.09.028>
- Foley JA, Defries R, Asner GP et al (2005) Global consequences of land use. *Science* 309:570–574. <https://doi.org/10.1126/science.1111772>
- Tarolli P, Sofia G (2016) Human topographic signatures and derived geomorphic processes across landscapes. *Geomorphology* 255:140–161. <https://doi.org/10.1016/j.geomorph.2015.12.007>
- Hooke RL (2000) On the history of humans as geomorphic agents. *Geology* 28:843. [https://doi.org/10.1130/0091-7613\(2000\)28%3C843:OTHOHA%3e2.0.CO;2](https://doi.org/10.1130/0091-7613(2000)28%3C843:OTHOHA%3e2.0.CO;2)
- Maaß A-L, Schüttrumpf H, Lehmkuhl F (2021) Human impact on fluvial systems in Europe with special regard to today's river restorations. *Environ Sci Eur* 33:1–13. <https://doi.org/10.1186/s12302-021-00561-4>
- Werther L, Mehler N, Schenk GJ et al (2021) On the way to the fluvial anthroposphere—current limitations and perspectives of multidisciplinary research. *Water* 13:2188. <https://doi.org/10.3390/w13162188>
- Brown AG, Lespez L, Sear DA et al (2018) Natural vs anthropogenic streams in Europe: history, ecology and implications for restoration, river-rewilding and riverine ecosystem services. *Earth Sci Rev* 180:185–205. <https://doi.org/10.1016/j.earscirev.2018.02.001>
- Broothaerts N, Swinnen W, Hoeffers R et al (2021) Changes in floodplain geo-ecology in the Belgian loess belt during the first millennium AD. *Neth J Geosci*. <https://doi.org/10.1017/njg.2021.9>
- Dotterweich M (2008) The history of soil erosion and fluvial deposits in small catchments of central Europe: Deciphering the long-term interaction between humans and the environment — A review. *Geomorphology* 101:192–208. <https://doi.org/10.1016/j.geomorph.2008.05.023>
- Hoffmann T, Thorndyraft VR, Brown AG et al (2010) Human impact on fluvial regimes and sediment flux during the Holocene: review and future research agenda. *Glob Planet Change* 72:87–98. <https://doi.org/10.1016/j.gloplacha.2010.04.008>
- Notebaert B, Broothaerts N, Verstraeten G (2018) Evidence of anthropogenic tipping points in fluvial dynamics in Europe. *Glob Planet Change* 164:27–38. <https://doi.org/10.1016/j.gloplacha.2018.02.008>

18. Verstraeten G, Broothaerts N, van Loo M et al (2017) Variability in fluvial geomorphic response to anthropogenic disturbance. *Geomorphology* 294:20–39. <https://doi.org/10.1016/j.geomorph.2017.03.027>
19. Chen Y, Xu Y, Yin Y (2009) Impacts of land use change scenarios on storm-runoff generation in Xitiao basin, China. *Quatern Int* 208:121–128. <https://doi.org/10.1016/j.quaint.2008.12.014>
20. Chen J, Li K, Chang K-J et al (2015) Open-pit mining geomorphic feature characterisation. *Int J Appl Earth Obs Geoinf* 42:76–86. <https://doi.org/10.1016/j.jag.2015.05.001>
21. Zhu D, Chen T, Zhen N et al (2020) Monitoring the effects of open-pit mining on the eco-environment using a moving window-based remote sensing ecological index. *Environ Sci Pollut Res Int* 27:15716–15728. <https://doi.org/10.1007/s11356-020-08054-2>
22. Flatley A, Rutherford I, Hardie R (2018) River channel relocation: problems and prospects. *Water* 10:1360. <https://doi.org/10.3390/w10101360>
23. Henselowsky F, Rölkens J, Kelterbaum D et al (2021) Anthropogenic relief changes in a long-lasting lignite mining area ('Ville', Germany) derived from historic maps and digital elevation models. *Earth Surf Proc Landf* 46:1725–1738. <https://doi.org/10.1002/esp.5103>
24. Syvitski J, Ángel JR, Saito Y et al (2022) Earth's sediment cycle during the Anthropocene. *Nat Rev Earth Environ* 3:179–196. <https://doi.org/10.1038/s43017-021-00253-w>
25. Costea M (2018) Impact of floodplain gravel mining on landforms and processes: a study case in Orlat gravel pit (Romania). *Environ Earth Sci*. <https://doi.org/10.1007/s12665-018-7320-y>
26. Kondolf MG (1994) Geomorphic and environmental effects of instream gravel mining. *Landsc Urban Plan* 28:225–243. [https://doi.org/10.1016/0169-2046\(94\)90010-8](https://doi.org/10.1016/0169-2046(94)90010-8)
27. Rinaldi M, Wyzga B, Surian N (2005) Sediment mining in alluvial channels: physical effects and management perspectives. *River Res App* 21:805–828. <https://doi.org/10.1002/rra.884>
28. Mossa J, James LA (2013) Impacts of mining on geomorphic systems. In: Shroder J, James LA, Harden CP et al (eds) *Treatise on geomorphology*, vol 13. Elsevier, San Diego, pp 74–95
29. Flatley A, Markham A (2021) Establishing effective mine closure criteria for river diversion channels. *J Environ Manage* 287:112287. <https://doi.org/10.1016/j.jenvman.2021.112287>
30. Vaillant Byzigiro R, Raab T, Maurer T (2015) Small-scale opencast mining: an important research field for anthropogenic geomorphology. *Erde* 146:213–231. <https://doi.org/10.12854/erde-146-21>
31. Gerwin W, Raab T, Birkhofer K et al (2023) Perspectives of lignite post-mining landscapes under changing environmental conditions: what can we learn from a comparison between the Rhenish and Lusatian region in Germany? *Environ Sci Eur* 35:1–24. <https://doi.org/10.1186/s12302-023-00738-z>
32. Elsner H (2022) Band II: Gewinnung in den Bundesländern. In: Elsner H (ed) *Bundesanstalt für Geowissenschaften und Rohstoffe. Sand und Kies in Deutschland*, Hannover
33. Lehmkuhl F, Schulte P, Römer W et al (2023) The loess landscapes of the Lower Rhine Embayment as (geo-)archeological archives—insights and challenges from a geomorphological and sedimentological perspective. *E&G Quat Sci J* 72:203–218. <https://doi.org/10.5194/egqsj-72-203-2023>
34. Zimmermann A (2012) Cultural cycles in Central Europe during the Holocene. *Quat Int* 274:251–258. <https://doi.org/10.1016/j.quaint.2012.05.014>
35. Landschaftsverband Rheinland und Landschaftsverband Westfalen-Lippe. *Kulturlandschaftsgenese von Nordrhein-Westfalen*. 2007.
36. Lehmkuhl F, Stauch G (2023) Anthropogenic influence of open pit mining on river floods, an example of the Blessem flood 2021. *Geomorphology* 421:108522. <https://doi.org/10.1016/j.geomorph.2022.108522>
37. Lehmkuhl F, Schüttrumpf H, Schwarzbauer J et al (2022) Assessment of the 2021 summer flood in Central Europe. *Environ Sci Eur* 34:1–6. <https://doi.org/10.1186/s12302-022-00685-1>
38. Tradowsky JS, Philip SY, Kreienkamp F et al (2023) Attribution of the heavy rainfall events leading to severe flooding in Western Europe during July 2021. *Clim Change* 176:1–38. <https://doi.org/10.1007/s10584-023-03502-7>
39. Lehmkuhl F, Stauch G, Schulte P et al. (2022) Enormous erosion in mining areas during the 2021 July flood in western Germany: Examples from the Inde and Erft River. *Copernicus Meetings*
40. Ahnert F (1989) The major landform regions 1. In: Ahnert F (ed) *Landforms and landform evolution in West Germany*, vol 15. CATENA, Cremlingen-Destedt, pp 1–10
41. Ahorner L (1962) Untersuchungen zur quartären Bruchtektonik der Niederrheinischen Bucht. *E&G Quat Sci J* 13:24–105. <https://doi.org/10.3285/eg.13.1.04>
42. Klostermann J. *Das Quartär der Niederrheinischen Bucht: Ablagerungen der letzten Eiszeit am Niederrhein*; mit 8 Tabellen. Zugl.: Münster, Univ., Habil.-Schr., 1991. Geolog. Landesamt Nordrhein-Westfalen, Krefeld. 1991.
43. Schulte P, Weber A, Keßels J et al (2024) Morphodynamics and heavy metal accumulation in an artificially built near-natural river (Inde, Germany). *J Sediment Environ* 9:117–133. <https://doi.org/10.1007/s43217-023-00160-8>
44. Maaß A-L, Esser V, Frings RM et al (2018) A decade of fluvial morphodynamics: relocation and restoration of the Inde River (North-Rhine Westphalia, Germany). *Environ Sci Eur* 30:40. <https://doi.org/10.1186/s12302-018-0170-0>
45. Junghänel T, Bissoli P, Daßler J et al. Hydro-klimatologische Einordnung der Stark- und Dauerniederschläge in Teilen Deutschlands im Zusammenhang mit dem Tiefdruckgebiet „Bernd“ vom 12. bis 19. 2021.
46. Mohr S, Ehret U, Kunz M et al (2023) A multi-disciplinary analysis of the exceptional flood event of July 2021 in central Europe—part 1: event description and analysis. *Nat Hazards Earth Syst Sci* 23:525–551. <https://doi.org/10.5194/nhess-23-525-2023>
47. Döscher N, Ketzler G, Leuchner M. Klimatologen blicken auf die Niederschlagsextreme. Eine klimageographische Perspektive auf das Starkregenereignis vom Juli. 2021. pp. 18–27. <https://doi.org/10.18154/RWTH-CONV-248108>
48. LANUV NRW. *ELSAS-Web—Oberflächengewässer Pegel*. 2023.
49. Weber A, Wolf S, Becker N et al (2023) The risk may not be limited to flooding: polluted flood sediments pose a human health threat to the unaware public. *Environ Sci Eur* 35:1–19. <https://doi.org/10.1186/s12302-023-00765-w>
50. James MR, Robson S, d'Oleire-Oltmanns S et al (2017) Optimising UAV topographic surveys processed with structure-from-motion: ground control quality, quantity and bundle adjustment. *Geomorphology* 280:51–66. <https://doi.org/10.1016/j.geomorph.2016.11.021>
51. Stauch G, Dörwald L, Esch A et al (2023) 115 years of sediment deposition in a reservoir in Central Europe: topographic change detection. *Earth Surf Proc Landf*. <https://doi.org/10.1002/esp.5722>
52. James MR, Antoniazza G, Robson S et al (2020) Mitigating systematic error in topographic models for geomorphic change detection: accuracy, precision and considerations beyond off-nadir imagery. *Earth Surf Proc Land* 45:2251–2271. <https://doi.org/10.1002/esp.4878>
53. Geologischer Dienst NRW (2023) Bohrungen in NRW: DABO. <https://www.bohrungen.nrw.de/>. Accessed 12 Nov 2023
54. Bezirksregierung Köln (2024) Historische Topographische Karten. <https://www.bezreg-koeln.nrw.de/geobasis-nrw/produkte-und-dienste/topographische-karten/historische-topographische-karten>. Accessed 15 Jan 2024
55. Bezirksregierung Köln (2019) Digitales Geländemodell: Geobasis NRW. <https://www.bezreg-koeln.nrw.de/geobasis-nrw/produkte-und-dienste/hoehenmodelle/digitale-gelaendemodelle/digitales-gelaendemodell>. Accessed 13 Nov 2023
56. Malcherek A (2019) Der Überfall über Wehre. In: Malcherek A (ed) *Fließgewässer*. Springer Fachmedien Wiesbaden, Wiesbaden, pp 175–203
57. Mahanta C, Saikia L (2016) Sediment dynamics in a large alluvial river: characterization of materials and processes and management challenges. In: Sharma N (ed) *River system analysis and management*. Springer, Singapore, pp 47–71
58. Hüljström F (1935) Studies of the morphological activities of rivers as illustrated by the river Fyris. *Bull Geological Institution of the University of Upsala* 25:221–227
59. LANUV NRW (2023) Überschwemmungsgebiete NRW. <https://www.gis-rest.nrw.de/atomFeed/rest/atom/01cbea15-f591-4030-ad33-cb59ce2e9d.html>. Accessed 12 Nov 2023
60. Zanke U (2013) Grundwasserhydraulik. In: Zanke U (ed) *Hydraulik für den Wasserbau*. Springer, Berlin, pp 71–94
61. Mohrlök U (2009) Bilanzmodelle in der Grundwasserhydraulik: Quantitative Beschreibung von Strömung und Transport im Untergrund. Teilw. zugl.: Karlsruhe, Univ., Habil. Universitätsverlag, Karlsruhe. 2008.

62. Wu W, Wang SSY (2006) Formulas for sediment porosity and settling velocity. *J Hydraul Eng* 132:858–862. [https://doi.org/10.1061/\(ASCE\)0733-9429\(2006\)132:8\(858\)](https://doi.org/10.1061/(ASCE)0733-9429(2006)132:8(858))
63. The engineering toolbox. Dirt and mud—densities. 2010. https://www.engineeringtoolbox.com/dirt-mud-densities-d_1727.html. Accessed 13 Nov 2023.
64. Vitz E, Moore JW, Shorb J et al. Density of rocks and soils. 2016. https://chem.libretexts.org/Ancillary_Materials/Exemplars_and_Case_Studies/Exemplars/Geology/Density_of_Rocks_and_Soils. Accessed 23 Jan 2024.
65. Wolf S, Klopries E, Schüttrumpf H et al (2023) Design values for dams exceeded: Lessons learnt from the flood event 2021 in Germany. In: Boes RM, Droz P, Leroy R (eds) Role of dams and reservoirs in a successful energy transition: Proceedings of the 12th ICOLD European Club Symposium 2023 (ECS 2023, Interlaken, Switzerland, 5–8 September 2023). CRC Press, Boca Raton, pp 418–427
66. Buchty-Lemke M, Lehmkuhl F (2018) Impact of abandoned water mills on Central European foothills to lowland rivers: a reach scale example from the Wurm River, Germany. *Geogr Ann Ser B* 100:221–239. <https://doi.org/10.1080/04353676.2018.1425621>
67. Flatley A, Rutherford I (2023) Establishing geomorphic reference criteria for design of river diversions around mine pits in the Pilbara, Western Australia. *Miner Water Environ* 42:293–311. <https://doi.org/10.1007/s10230-023-00937-3>
68. Roberts ME, Burrows RM, Thwaites RN et al (2022) Modelling classical gullies—a review. *Geomorphology* 407:108216. <https://doi.org/10.1016/j.geomorph.2022.108216>
69. Kisseler E, Wolf S, Sauter H, Schüttrumpf H (2023) Reduktion der Vulnerabilität gegenüber Hochwasser – Empfehlungen zur Flächennutzung auf Basis von Flutmarken des Juli-Hochwassers 2021. Reduktion der Vulnerabilität gegenüber Hochwasser – Empfehlungen zur Flächennutzung auf Basis von Flutmarken des Juli-Hochwassers 2021. 2023:498–506. <https://doi.org/10.3243/kwe2023.08.003>
70. Kirkby MJ, Bracken LJ (2009) Gully processes and gully dynamics. *Earth Surf Processes Landf* 34:1841–1851. <https://doi.org/10.1002/esp.1866>
71. Bennett SJ, Alonso CV, Prasad SN et al (2000) Experiments on headcut growth and migration in concentrated flows typical of upland areas. *Water Resour Res* 36:1911–1922. <https://doi.org/10.1029/2000WR900067>
72. Flores-Cervantes JH, Istanbuluoglu E, Bras RL (2006) Development of gullies on the landscape: a model of headcut retreat resulting from plunge pool erosion. *J Geophys Res*. <https://doi.org/10.1029/2004JF000226>
73. Wilson G (2011) Understanding soil-pipe flow and its role in ephemeral gully erosion. *Hydrol Process* 25:2354–2364. <https://doi.org/10.1002/hyp.7998>
74. Nichols MH, Nearing M, Hernandez M et al (2016) Monitoring channel head erosion processes in response to an artificially induced abrupt base level change using time-lapse photography. *Geomorphology* 265:107–116. <https://doi.org/10.1016/j.geomorph.2016.05.001>
75. Mohren J, Ritter M, Binnie SA et al. (2022) Erosion of arable land during the July 2021 flood event in Erfstadt-Blessem, Germany: understanding groundwater sapping
76. Clostermann M, Lisiecki BR (2022) Sachstandsbericht zur Südböschung der Kiesgrube Blessem: Erkenntnisstand 03/2022
77. Choi Y, Park H-D, Sunwoo C (2008) Flood and gully erosion problems at the Pasir open pit coal mine, Indonesia: a case study of the hydrology using GIS. *Bull Eng Geol Environ* 67:251–258. <https://doi.org/10.1007/s10064-008-0131-8>
78. Bai Y, Guo M, Kang H et al (2021) Morphodynamics of gully development on the platform-slope system of spoil dumps under platform concentrated flow. *Land* 10:1270. <https://doi.org/10.3390/land10111270>
79. Lowry J, Narayan M, Hancock GR et al (2019) Understanding post-mining landforms: utilising pre-mine geomorphology to improve rehabilitation outcomes. *Geomorphology* 328:93–107. <https://doi.org/10.1016/j.geomorph.2018.11.027>
80. Hancock GR, Willgoose GR (2021) Predicting gully erosion using landform evolution models: insights from mining landforms. *Earth Surf Proc Landf* 46:3271–3290. <https://doi.org/10.1002/esp.5234>
81. Reed M, Kite S (2020) Peripheral gully and landslide erosion on an extreme anthropogenic landscape produced by mountaintop removal coal mining. *Earth Surf Proc Landf* 45:2078–2090. <https://doi.org/10.1002/esp.4867>

Publisher's Note

Springer Nature remains neutral with regard to jurisdictional claims in published maps and institutional affiliations.